Dynamics of particle trajectories in a Rayleigh–Bénard problem

C. Simó [a], D. Puigjaner [b,*], J. Herrero [c] and F. Giralt [c]

[a] *Dept. de Matemàtica Aplicada i Anàlisi, Univ. de Barcelona, Barcelona, Catalunya, Spain*
[b] *Dept. Enginyeria Informàtica i Matemàtiques, Univ. Rovira i Virgili, Tarragona, Catalunya, Spain.*
[c] *Dept. Enginyeria Qumica, Univ. Rovira i Virgili, Tarragona, Catalunya, Spain.*

Abstract

Fluid particle trajectories for the Rayleigh–Bénard problem in a cube with perfectly conducting lateral walls have been investigated. The velocity and temperature fields of the stationary flow solutions have been obtained by means of a parameter continuation procedure based on a Galerkin spectral method. The rich dynamics of the resulting fluid particle paths has been studied for three branches of stationary solutions and different values of the Rayleigh number within the range $10^4 \leq Ra \leq 1.5 \times 10^5$ at a Prandtl number equal to 130. The stability properties and bifurcations of fixed points, which play a key role in the global dynamics, have been analyzed. Main periodic orbits and their stability character have also been determined. Poincaré maps reveal that regions of chaotic motion and regions of regular motion coexist inside the cavity. The boundaries of these three–dimensional regions have been determined. The metric entropy gives an indication of the mixing properties of the large chaotic zone.

Key words: Chaotic advection, Rayleigh-Bénard convection, Dynamical systems
PACS: 05.45.Pq, 47.52.+j, 47.55.P-

1. Introduction

The determination and control of fluid mixing efficiency is an important issue in many engineering applications. Although efficient mixing is usually related to turbulent regimes there are several industrial applications that require an efficient mixing in the absence of turbulence or high shear stresses. In such cases, concepts and tools from dynamical

* Corresponding author.
Email addresses: carles@maia.ub.es (C. Simó), dolors.puigjaner@urv.cat (D. Puigjaner), joan.herrero@urv.cat (J. Herrero), fgiralt@urv.cat (F. Giralt).

systems theory can be applied to understand the mixing process. While the pioneering work of Reynolds connected fluid mixing and chaos theory [1] it was not until the seminal paper of Aref [2] that a mixing fluid flow problem was thoroughly studied from a dynamical systems perspective. Aref [2] introduced the term chaotic advection to refer to the complex behavior that a passive fluid particle, or a passively advected scalar quantity such as temperature or concentration can attain as it moves with the flow. Chaotic advection has received significant attention in recent years ([3], [4],[5], [6], [7], [8], [9], [10], [11]) because of its impact on both transport and mixing properties in many fluid flow systems.

Passive fluid advection is described by the Lagrangian representation of fluid motion. Even when the fluid flow is laminar and steady and the Eulerian velocity at any given point in space is fixed, the trajectories of passive particles may exhibit rich chaotic dynamics (i.e., trajectories of two arbitrarily close points in space may separate exponentially in time). Mixing induced by molecular diffusion in chaotic regions of the flow, is often negligible compared to the mixing induced by the flow dynamics. It is known that mixing is enhanced when the levels of chaos in the flow domain increase [7]. On the other hand, the existence of regions of regular motion, characterized by the presence of islands in two dimensional (2D) maps and nested KAM–tori in three-dimensional (3D) flows, form a barrier that prevents fluid inside the regular region from mixing with the outside fluid. Hence, the global geometrical viewpoint of dynamical systems theory can be very useful in the understanding of qualitative and quantitative aspects of fluid motion.

The main objective of the current work is to present some preliminary results on the application of dynamical systems tools to the analysis of the rich dynamics of particle trajectories in a particular 3D, volume–preserving, fluid flow system. The fluid flow problem investigated is the natural convection (Rayleigh-Bénard) inside a cubical cavity heated from below, with perfectly conducting lateral walls. The bifurcation diagram of steady convective flow patterns in this flow system, recently reported by Puigjaner et al. [12], reveals the existence of four and nine different stable complex flow patterns in the range $Ra < 1.5 \times 10^5$ at $Pr = 0.71$ and 130, respectively. The complexity of the bifurcation diagrams is especially noticeable at $Pr = 130$, where all solutions branches that set in at bifurcations from the conductive solution, except for the single roll denoted as B_1, are connected to each other through their subsequent bifurcations [12].

The present study focuses on the analysis of three particular steady flow patterns, denoted as B_2, B_{25} and B_{251}, at $Pr = 130$. The choice of these three flow patterns was motivated by their connection in the bifurcation diagram through symmetry–breaking bifurcations and by the complex evolution of the spatial configuration of the B_2 flow pattern as the Rayleigh parameter increased. Moreover, all three flow patterns are stable within certain ranges of Ra in the studied domain. To explore the dynamics of these three flow patterns several tools, such as Poincaré sections, critical–point analysis, periodic orbits and Lyapunov exponents have been used. Some topological relations have also been considered in order to check the results obtained. The symmetries of the solutions have been exploited to obtain invariant closed surfaces where the velocity field is everywhere tangent to the surface. Invariant surfaces are particularly important because they separate the domain into non–communicating regions, that is, into regions between which there is no transport. In the current work the dynamics of the flows restricted over invariant surfaces have been analyzed with the objective to obtain useful knowledge about the global flow dynamics. In addition, the effect of the Rayleigh number on the number and type of critical points and on the formation and persistence of regions with regular motion has been investigated. The metric entropy has been used as a quantitative measure of the mixing properties of the flow.

2. Problem formulation and numerical methods

2.1. *Flow System*

An incompressible steady flow of a Newtonian fluid confined in a cube with six rigid walls is studied. The top and bottom horizontal walls are kept at constant temperatures T_c and T_h ($T_c < T_h$), respectively, and the four lateral walls are assumed to be perfectly conducting, i.e., a linear vertical temperature profile is assumed. The domain, shown in figure (1), is scaled by the length of the side of the cube L and is represented by $\Omega = [-1/2, 1/2]\times[-1/2, 1/2]\times[-1/2, 1/2]$. The problem is governed by the 3D incompressible Navier–Stokes equations and the energy conservation equation. The flow within the cavity depends on two non–dimensional parameters, the Rayleigh number, Ra, and the Prandtl number, Pr. These parameters are defined as $Ra = \beta(\Delta T)gL^3/\alpha\nu$ and $Pr = \nu/\alpha$, where g is the acceleration of gravity, β is the coefficient of thermal expansion, ν is the kinematic viscosity, α is the thermal diffusivity and $\Delta T = T_h - T_c$. The Prandtl number ($Pr = 130$) is chosen to match silicone oil.

2.2. *Velocity field and bifurcation diagram*

The numerical method followed elsewhere ([12]–[13]) to obtain steady solutions of the Boussinesq approximation of the governing equations is briefly described here. Calculations were based on a Galerkin spectral method with a complete, divergence-free set of basis functions. Once the velocity and temperature fields were approximated by truncated expansions in terms of the basis functions, the partial differential governing equations were transformed into a system of ordinary differential equations whose unknowns were the coefficients in the expansions. A continuation procedure was applied to determine steady solutions at different Rayleigh numbers. The bifurcations and stability character of the solutions were determined along the different tracked solution branches. A total set of 11076 basis functions were typically used in the calculations. The symmetry properties of the solutions along a bifurcation branch, when they exist, were exploited to reduce the number of needed basis functions by a factor of two or four. The accuracy assessment of the Galerkin method and comparisons between the results obtained with the Galerkin method and different numerical and experimental studies reported in the literature can be found in references [12], [14] and [13].

2.3. *Particle trajectories and critical points*

Given a steady flow velocity field $\mathbf{U} = (u_1, u_2, u_3)$, calculated with the numerical method described above, the particle trajectories or streamlines of non–diffusive passive particles are the solutions of the following advection equations:

$$\dot{x_1} = u_1(x_1, x_2, x_3), \quad \dot{x_2} = u_2(x_1, x_2, x_3), \quad \dot{x_3} = u_3(x_1, x_2, x_3)\,. \tag{1}$$

Critical or equilibrium points are fixed points of the differential equation (1) (i.e., points where all three velocity components vanish). Qualitative analysis of the flow in the neighborhood of critical points provides relevant information about the local flow topology. Critical points on the wall surface are also of interest because they indicate flow separation or flow attachment when shear stress equals zero. A critical point is non–degenerate if the linear expansion of the velocity field about the point has not zero as an eigenvalue; otherwise the critical point is degenerate. In particular, every point on a non–slip boundary is a degenerate critical point. To remove the degeneracy and to isolate the critical points on the walls of the cube the velocity field was rescaled to extend continuously to the boundaries with a non–zero value there. Let $b = (b_1, b_2, 0)$ be the spatial coordinates of a point at the wall defined by the equation $x_3 = 0$, and let us assume that b is not at an edge of the cube. Substituting the velocity field in equation (1) by the second order Taylor expansion of the velocity about the point b, rescaling the time and using the divergence-free condition yields,

$$\begin{aligned} \frac{dx_i}{d\tau} &= \frac{\partial u_i}{\partial x_3} + \frac{\partial^2 u_i}{\partial x_3 \partial x_1}(x_1 - b_1) + \frac{\partial^2 u_i}{\partial x_3 \partial x_2}(x_2 - b_2) + \frac{1}{2}\frac{\partial^2 u_i}{\partial x_3^2} x_3 \quad i = 1, 2\,, \\ \frac{dx_3}{d\tau} &= -\frac{1}{2}\left(\frac{\partial^2 u_1}{\partial x_1 \partial x_3} + \frac{\partial^2 u_2}{\partial x_2 \partial x_3}\right) x_3\,, \end{aligned} \tag{2}$$

where $\tau = x_3 t$ is the rescaled time. The limiting streamlines to the wall $x_3 = 0$ (i.e., the trajectories of particles passing very close to the wall) are obtained by taking the limit $(x_1, x_2, x_3) \to (b_1, b_2, 0)$ in equations (2),

$$\frac{dx_i}{d\tau} = \frac{\partial u_i}{\partial x_3} \quad i = 1, 2\,. \tag{3}$$

Since the vorticity field $\mathbf{W} = (w_1, w_2, w_3)$ at the wall $x_3 = 0$ satisfies

$$w_1 = -\frac{\partial u_2}{\partial x_3},\ w_2 = -\frac{\partial u_1}{\partial x_3},\ w_3 = 0\,,$$

equation (3) can be written in terms of vorticity field as

$$\frac{dx_1}{d\tau} = w_2, \quad \frac{dx_2}{d\tau} = -w_1\,. \tag{4}$$

Hence, the isolated critical points at the boundary have zero vorticity. Comparison of equations (3) and (4) shows that limiting streamlines are orthogonal to vortex lines at the boundary. Analogous arguments can be applied to obtain the limiting streamline equations associated to the rest of walls and to the edges. It should be remarked that third order Taylor expansions are needed in the case of edges.

Streamlines and limiting streamlines were respectively calculated by integrating in time equations (1) and (3) or their analogous at other walls of the cavity. In both cases, a seventh-eighth order Runge–Kutta–Fehlberg (RK78) method was used. In all the current calculations the local error tolerance in the RK78 procedure was set to 10^{-12}. Each one of the components in (1) consists of sums with thousands of terms, as mentioned in section 2.2.

In the context of fluid mechanics non–degenerate critical points on the boundary (i.e., non-degenerate fixed points of equations (3) and their analogous ones at the other walls of the cube) are referred as attachment points if they have a stable direction from the interior of the domain to the wall and separation points if they have an unstable direction from the wall to the interior of the domain. Critical points in the interior of the domain are called stagnation points and the limiting streamlines on the boundary are named skin friction lines.

The location of critical points in the interior of the domain was determined by means of a Newton method that solved numerically the system of equations $\mathbf{U} = 0$. A set of initial points for the Newton iterations was generated by defining a uniform grid with $n \times n \times n$ volume cells and setting the coordinates of the center of each cell as initial values. It was expected that for a sufficiently fine grid none of interior fixed points will be missed (a value of $n = 41$ has proved to be high enough in all of the cases investigated). See 2.3.2 for the checks performed. Similarly, the location of degenerate critical points at the cavity walls were determined by solving numerically the system of equations $\mathbf{W}_t = 0$, starting at points on a uniform grid, where $\mathbf{W}_t$ is the vector with the two components of vorticity that are tangent to the wall. Finally, degenerate critical points at an edge parallel to the x_i coordinate axis were located by solving the equation

$$\frac{\partial^2 u_i}{\partial x_j \partial x_k} = 0, \quad j, k \neq i \tag{5}$$

by means of the Newton method and by providing a set of n initial values uniformly distributed along the edge.

2.3.1. *Local behavior near critical points*

Let λ_1, λ_2, λ_3 be the eigenvalues associated to the linearization of the vector velocity field about a critical point x_c. Since the studied flow is divergence–free as it preserves volume, the following relations hold:

$$\begin{aligned}
&\lambda_1 + \lambda_2 + \lambda_3 = 0 && \textit{if } x_c \textit{ is in the interior of the cube};\\
&\frac{1}{2}(\lambda_1 + \lambda_2) + \lambda_3 = 0 && \textit{if } x_c \textit{ is on a wall of the cube };\\
&2(\lambda_1 + \lambda_2) + \lambda_3 = 0 && \textit{if } x_c \textit{ is on an edge of the cube;}
\end{aligned} \tag{6}$$

The eigenvector associated to the λ_3 eigenvalue in (6) is the direction of the edge when x_c is at an edge and it is not tangent to the wall when x_c is at a wall. As a consequence of (6), the critical points can be classified into the following four types: (i) **SF** (stable focus with a 1D unstable manifold), (ii) **UF** (unstable focus with a 1D stable manifold), (iii) **2S** (saddle with a 2D stable manifold) and (iv) **1S** (saddle with a 1D stable manifold). It is worth to note that the critical points that are located at an edge are always saddles because the linearization about a critical point x_c at an edge yields three real eigenvalues.

2.3.2. *Topological checks*

The Poincaré–Hopf index theorem has been used to check the number and type of critical points obtained with the numerical method described above. The Poincaré–Hopf index theorem states that the sum of the Poincaré indexes over all the isolated critical points of a vector field on a compact orientable differentiable manifold is equal to the Euler characteristic of the manifold. The key step in applying this topological result to the current study is to pass from the cubical domain to the 3D sphere $\mathbb{S}^3$, whose Euler characteristic is zero. To perform the conversion we first observe that the interior of the cubical domain is topologically equivalent to a 3D open ball B^3 and its boundary is equivalent to a 2D sphere $\mathbb{S}^2$. Second, B^3 is deformed to become a 3D hemisphere whose equator is $\mathbb{S}^2$. Finally $\mathbb{S}^3$ is obtained by taking a symmetric copy of the 3D hemisphere and gluing both hemispheres after identifying the $\mathbb{S}^2$ boundaries. Note that the critical points located in the interior of the cube must be counted twice in the Poincaré–Hopf theorem because of the symmetrizing procedure. On the other hand, the critical points located on an edge whose eigenvalues λ_1 and λ_2 satisfy $\lambda_1\lambda_2 < 0$ must not be counted in the Poincaré–Hopf theorem. These points do not play any role in the dynamics of particle trajectories because fluid neither enters to nor leaves from them. Note that the eigenvectors corresponding to the λ_1 and λ_2 eigenvalues are at one of the two walls adjacent to the edge, whereas the eigenvector associated to the λ_3 eigenvalue is parallel to the edge. The behavior of the flow near edges can also be easily studied by a local change of coordinates, transforming the two edge faces into a flat surface ("opening" the corner by doubling angles). The Poincaré index of a critical point x_c satisfying $Re\lambda_i \neq 0,\ i = 1, 2, 3$ is $(-1)^{n_p}$, where $n_p = \#\{\lambda_i \mid Re\lambda_i < 0,\ i = 1, 2, 3\}$. In order to ensure that no critical point is missed the Poincaré–Hopf condition has been checked thorough at all calculations performed.

2.4. *Poincaré sections, Lyapunov exponents and measure of chaotic regions*

The global dynamics of the flows considered is most clearly analyzed by studying one or more associated Poincaré maps. A Poincaré map is obtained by considering the intersections of several particle trajectories with a certain lower dimensional subspace, called the Poincaré section. Poincaré maps are useful to distinguish well–mixed chaotic regions from unmixed regular regions in the flow and to qualitatively identify changes in the shape of these regions as one or more parameters vary. In the present study the nine horizontal planes $x_3 = -0.5 + 0.1k,\ k = 1, \cdots, 9$ have been used as Poincaré sections. The associated Poincaré maps have been calculated by integrating the trajectories of 512 fluid particles equidistributed within the cavity up to times equal to 10^3. The symmetry properties of the solutions have been used to reduce the computation workload.

A quantitative analysis of the mixing efficiency of a given flow pattern can be obtained by computing the maximal Lyapunov exponent L_M. Lyapunov exponents are related to the specific stretching rate and mixing efficiency of the fluid flow system. An increase of the level of Lagrangian chaos implies an increase in the measure of the set of orbits with positive maximal Lyapunov exponent. The local maximal Lyapunov exponent associated to an initial point x_0 is defined as

$$L_M(x_0) = \lim_{t\to\infty} \frac{1}{t} \log\left(\frac{\parallel l_t \parallel}{\parallel l_0 \parallel}\right),$$

assuming that the limit exists, where l_t is the image after a time t of an arbitrary vector l_0 that evolves under the variational equations. Thus, given a solution $\phi(t, x_0)$ of the differential equations (1) with initial condition $\phi(0, x_0) = x_0$, l_t is defined as $l_t = D_x\phi(t, x_0)l_0$. In the present study, the maximal Lyapunov exponent has been estimated by averaging finite time approximations of $L_M(x_0)$ for 49 equidistributed initial conditions on the vertical plane $x_2 = 0.48$. The final integration time has been set to 10^5 and the results obtained for times lower than 10^4 have not been taken into account in the calculation as they have been considered as transitory stages. More concretely, the quotients $\log\left(\| l_t \| / \| l_0 \|\right)/t$ have been computed every 10^3 units of time after the transient. These quotients are averaged with respect to all these times and all the initial conditions. The appropriateness of the time–steps and partial samples used to evaluate the quotients has been checked. Furthermore all the quotient computed are very similar, with very few exceptions which are identified as corresponding to orbits which spend some thousands of units of time close to an invariant torus.

Regular regions, characterized by the presence of nested invariant tori, represent an important obstacle to efficient mixing. Consequently, the knowledge of the shape and size of regions with regular flow motion would be determinant in predicting the mixing efficiency of the flow. Based on the trajectories of several initial conditions we have developed an algorithm to estimate the shape and size of these regular regions. The key ideas of the algorithm are: (i) the cubical cavity is divided into $n \times n \times n$ equally sized cubic cells; (ii) for each initial condition x_0 in a certain set C_I, the trajectory described by a fluid particle initially located at x_0 is calculated by numerically integrating equation (1); (iii) at each integration time step, the cubic cells that have been visited by one or more fluid particle trajectories are stored; (iv) the number of cells $N_r(t)$ that at time t have not yet been visited by any particle trajectory is calculated for any t multiple of the selected Δt; (v) the procedure is stopped when the integration time exceeds a maximum integration time t_M. It should be noted that motion is very slow close to the boundaries of the domain. An analysis of the limit streamlines shows that no invariant torus is too close to the boundaries. To prevent points close to the boundaries from being considered as points set on a regular region, all points at a distance less than 0.01 from the boundaries are considered as non-regular.

The set C_I and the values of n, Δt and t_M must be properly selected to obtain good convergence of N_r. The set

$$C_I = \{(-0.375 + i/4, 0.48, -0.375 + j/4)\,,\ i, j = 0, \cdots, 6\}$$

and the values $n = 200$, $\Delta t = 200$ and $t_M = 10^6$ were selected in the current study. It has been checked that with these choices the values of $N_r(t)$ are almost constant between $\frac{3}{4}t_M$ and t_M. It is worth to note that the symmetry properties of the studied flow patterns were used to reduce the calculations.

From now on we shall talk loosely of the “chaotic zone” as the set of points in the cubical domain which are outside invariant tori. Of course, there are small chaotic zones bounded by tori, but they hardly contribute to the mixing. When a flow pattern presents an invariant symmetry plane this plane will separate the domain into two symmetric non–communicating regions (i.e., into two regions without transport between them). There is numerical evidence that the chaotic zone in each of these non–communicating regions is connected and that the value of L_M is constant on them. This fact has been used in the computation of $N_r(t)$.

To have a quantitative measure of the mixing properties it is not enough to estimate the maximal Lyapunov exponent. The volume V_c occupied by the chaotic zone also plays a role. This suggests using the metric entropy h_m (see [15] for a definition) as a suitable indicator of the mixing properties. According to the celebrated Pesin’s formula and taking into account the constant value of L_M on the chaotic zone, one has simply $h_m = L_M \times V_c$. Anyway this value is very similar to L_M because V_c is close to 1 in all the cases we have studied.

3. Results and discussion

The bifurcation diagram of the more relevant stable steady solutions developed inside a cubical cavity with perfectly conducting lateral walls and filled with silicone oil ($Pr = 130$) is shown in figure 2. This figure depicts the branches of the seven steady solutions, denoted as B_1, B_2, B_3, B_5, B_{25}, B_{34} and B_{251} by Puigjaner et. al [12], in the $(10^{-3}Ra, Nu - 0.012Ra^{1/2})$ parameter space. The Nusselt number Nu refers to the dimensionless convective heat transfer coefficient and was calculated as,

$$Nu = 1 - \int_{-0.5}^{0.5}\int_{-0.5}^{0.5} \frac{\partial\theta}{\partial z}(x, y, -0.5)dx\,dy\,, \tag{7}$$

being θ the temperature departure from the motionless conductive state. For the sake of clarity the variable $Nu - 0.012Ra^{1/2}$ is used as ordinate instead of Nu in figure 2. Those parts of the B_2, B_{25} and B_{251} solution branches that are the object of the current study are highlighted with a thick line in this figure. The symmetry properties and the ranges of stability of these three solutions are shown in table 1.

Figure 2 shows that the initially unstable B_2 solution becomes stable at $Ra = 67\,730$ and it remains stable until a symmetry-breaking bifurcation occurs at $Ra = 85\,694$. Since the B_{251} solution presents a turning point at $Ra = 48\,116$ two solution branches are possible for $Ra > 48\,116$. Figure 2 also shows that the stable solution that develops at this symmetry-breaking bifurcation point, denoted as B_{25}, connects the B_2 solution with the upper branch of the solution denoted as B_{251}. The B_2–B_{251} connection causes a transfer of stability from the S_{d_-} invariant B_2 solution to the S_y invariant B_{251} solution. An Eulerian analysis of the problem establishes that the B_2 flow pattern changes from a single diagonal roll configuration at $Ra = 10^4$ to a double toroidal configuration at $Ra = 8.5 \times 10^4$, as shown in figure 3. This figure shows zero surfaces of the second largest eigenvalue (Λ_2) of the tensor $S^2 + \Omega^2$, formed from the symmetric (S) and antisymmetric (Ω) parts of the velocity gradient tensor, (see reference [16] for details and discussion of the visualization method). Figure 3 also shows that the configuration of B_2 at $Ra = 85\,000$ is very similar to that of the B_{251} at $Ra = 10^5$, despite their different symmetry properties in table 1.

A preliminary investigation of the effect of varying the Rayleigh number on the Lagrangian dynamics of particle trajectories was carried out by examining the evolution of Poincaré maps along those parts of the B_2, B_{25} and B_{251} solutions plotted with a thick line in figure 2. Starting at $Ra = 10^4$, 119, 4 and 66 sample solutions on the B_2, B_{25} and B_{251} branches, respectively, were analyzed. The selected solutions on each branch were numbered consecutively following the solution branch. Thus, each solution can be identified either by its number n or by its corresponding Rayleigh number, Ra_n. Consecutive solutions were chosen so that $\mid Ra_{n+1} - Ra_n \mid = 10^3$; the only exception was near the two turning points on the B_2 solution where more frequent solutions were considered.

3.1. *Poincaré sections, periodic orbits and regular regions*

A very small selection of the computed Poincaré maps is shown in figure 4. Even though the few cases included in this figure are insufficient to obtain a global picture of the flow pattern evolution, they are useful to identify some relevant features and trends. Some characteristic symmetries of the solutions are also clearly evident in figure 4 where black (resp. grey) dots have been used for intersection of orbits with a constant value of z going up (resp. down). Figure 4(a) reveals the existence of four symmetric regions of regular motion surrounded by regions with chaotic motion at $Ra = 10^4$. The complex topology of these regular regions is more evident in figure 4(b), where period–three islands and a central elliptic region are clearly visible at $Ra = 3.3 \times 10^4$. Poincaré maps on both sections $z = 0$ and $z = 0.4$ are respectively shown in figures 4(c) and (d) at $Ra = 6 \times 10^4$. The latter figure is included to show the existence of four additional regions of regular motion. As these regions do not intersect the horizontal midplane $z = 0$ they cannot be identified in figure 4(c). Further details about the size and shape of regular regions are given below. The elliptic points at the center of the regular regions correspond to stable periodic solutions and are surrounded by regular KAM–tori which act as barriers for transport. The evolution of these elliptic points along the solution branch has been studied. A continuation method has been used to obtain the coordinates of these elliptic points and to analyze their stability character as a function of Ra. Due to the symmetries of the B_2 solution it was sufficient to study only one of the four elliptic points shown in figure 4. The Poincaré map associated to any transversal section S preserves the measure $\mathbf{U} \cdot dS$ because of the volume preserving condition of the current flow.

Figure 5 shows the evolution of the x-coordinate of the elliptic point along the solution branch. Since the solution branch presents two turning points, the number of solution, which is an integer between 1 and 119, is used as ordinate in this figure. The differential of the Poincaré map evaluated on the elliptic point presents a pair of complex conjugate eigenvalues of modulus one, as expected. The variation of the argument of these eigenvalues is shown in figure 5. Horizontal lines at $y = 2\pi/k,\ k = 2, \cdots, 7$ have been included in this figure because those points in the argument curve that intersect with the line $y = 2\pi/k$ mark the origin or end of islands of period k, as it is well known from the analysis of the normal form. Figure 5 also includes the evolution of the trace, Tr, of the differential of the Poincaré map on the elliptic point. Note that as the two eigenvalues are conjugated complex, the trace is twice the real part of the corresponding complex eigenvalues. Figure 5 reveals that a significant variation in the features of the elliptic point occurs at $Ra = 6 \times 10^4$, $(n = 51)$. Our hypothesis is that this variation is associated to the change in the stability character of the critical point located at the center of the cube. Critical points and their bifurcations are discussed below. Future research will be oriented to prove this hypothesis.

Poincaré maps shown in figure 4 reveal the existence of points on the chosen Poincaré sections where the flow is not transversal to the section. Since these points are points where the vertical velocity component vanishes they can be clearly identified in figure 4 as points that separate the regions where the flow raises (black points) from those regions where the flow falls down (grey points). In addition, figure 4(f) shows that the dynamics of particle trajectories corresponding to the B_{251} solution at $Ra = 10^5$ is rather similar to that shown in figure 4(e) for the B_2 solution at $Ra = 8.5 \times 10^4$, but the volume of the domain of motion bounded by tori at $Ra = 10^5$ becomes negligible. All the studied characteristics of the B_{25} and B_{251} are very similar to those corresponding to the B_2 solution at $Ra = 8.5 \times 10^4$. Consequently, the current discussion of results is centered on the B_2 solution branch.

Figure 6(a) shows that even at the first analyzed solution ($Ra = 10^4$) the fluid motion for the B_2 solution is largely chaotic. The percentage of region where chaotic motion develops is always above 82% and it increases rapidly from 85% to 98% with a fluctuating pattern. from 85% to 98%. This figure also shows, that despite the fluctuations, the size of chaotic region tends to increase with Ra, in agreement with the information inferred from the calculated Poincaré sections. Figure 6(b) depicts the metric entropy h_M as a function of the orbit number. Taking into account the relatively small variation of V_c the plot is similar to the one of L_M. Regions inside the cube where the flow motion is regular are plotted in figure 7 for Ra 10^4, 3.4×10^4, 6×10^4 and 8.5×10^4. The presence of two additional spherical–like regions of regular motion at $Ra = 6 \times 10^4$ ($n = 51$) in figure 7(c) produces a relative minimum in the percentage of chaotic motion in figure 6. The existence of these additional regular regions is also evident in figure 4(d). Their origin is related to a bifurcation where a pair of new critical points develop. This is discussed in section 3.2 and a description of the corresponding dynamics is given below. Figure 6 shows that chaotic region tends to increase its size with Ra. However, the maximal Lyapunov exponent does not follow the same trend as it behaves in the opposite way from $Ra = 6.3 \times 10^4$ ($n = 54$) and it decreases quasi monotonically from $Ra = 5.1 \times 10^4$ ($n = 84$), just after the second turning point occurs.

Figure 6(a) also provides interesting information on the dynamics. Let us consider $1 - V_c$, the measure of the domain bounded by invariant tori. That domain has several connected components. Beyond the largest domain around the family of periodic orbits discussed above, there are narrow domains around other periodic orbits, as can be seen in figures 7 (b,d). Relevant regular domains like the ones with spherical shape in figure 7(c) can also develop. It is worth to note, that results not shown here reveal that each spherical–like regular regions become two separated tori as Ra is increased from 6×10^4 to 6.1×10^4 and that similar smaller spherical–like regular regions develop at $Ra = 6.3 \times 10^4$. In all the cases the largest connected components of the regular region are associated to the discussed periodic orbits whose main features are plotted in figure 5. The other components can be related to bifurcations of these orbits. In particular, the narrow tori in figure 7(c) are related to the 3–periodic islands shown in figure 4(b). It is known that whenever the trace, Tr, of the Jacobian matrix associated to a periodic orbit takes values $Tr = 2\cos(2\pi m/k)$ k-periodic families of orbits bifurcate, either for increasing or decreasing values of Ra, depending on the sign of the first Birkhoff coefficient of the elliptic point of the Poincaré map. Generically 2 families appear: one elliptic and the other hyperbolic. When this k-periodic elliptic orbit of the Poincaré map moves away from the central elliptic point, it is surrounded by invariant islands. These ones, in turn, are surrounded by invariant rotational curves (i.r.c.) which enclose all the islands. The points in the confined region associated to the homoclinic tangle created by the k-periodic hyperbolic orbit can escape when the outer of these i.r.c. breaks down. In figure 6(a) the value of V_c ($100 - V_c$ in terms of the percentage of the regular region) has a sudden increase (decrease) between $n = 22$ and $n = 23$. It corresponds to the destruction of i.r.c. around period-3 islands. But other similar changes can be observed around $n =$ 2, 6, 11, 15, etc, associated to destruction of i.r.c. around islands of periods 6, 5, 4, 7, etc. Some reverse mechanisms have been also observed: an i.r.c. around some islands can reappear as n is increased. Note that since bifurcations from the central elliptic point depend only on the rotation number and the first Birkhoff coefficients associated to that point, they are a local phenomenon. In contrast, the creation and destruction of i.r.c. is a global phenomenon. Details on these mechanisms in other examples and their "universal" character will appear elsewhere [17].

Let us comment also on the spherical-like regions of regular motion beyond the discussion on critical points in 3.2. A fixed point P on the invariant symmetry plane Π, defined by $x+y=0$, has eigenvalues $2a, -a \pm ib$ with $a>0$. At a critical Ra_c the value a passes through zero and becomes negative. A periodic orbit is then created by a Hopf–pitchfork bifurcation on Π. Simultaneously two fixed points Q_1, Q_2 are created, close to P, one at each side of Π. The point P becomes an unstable focus with one stable direction and Q_1, Q_2 are stable foci with one unstable direction. The periodic orbit is attracting in Π and has an unstable direction transversal to Π. An analysis of the normal form shows, as usual, that it is rotationally invariant and integrable to all orders. For the normal form, the 2 branches of the 1D stable manifold of P go to Q_1 and Q_2, respectively, and the 2D stable manifolds of Q_1, Q_2 coincide with the unstable manifold of the periodic orbit. This coincidence would produce a spherical-like invariant domain. For the true system the manifolds do not coincide, but they miss coincidence by exponentially small quantities in $Ra - Ra_c$. Figure 8 shows an orbit started very close to Π near P. It approaches the periodic orbit, moves close to its 2D unstable manifold until reaching the vicinity of Q_1 and returns close to P. Note that for some range of Ra the splitting of the manifolds is so small that the spherical-like domain seems truly invariant.

Figure 9 (a) shows that the projection of a particle trajectory onto the plane $z=0$ tends to fill almost all the region $x+y \leq 0$ at $Ra = 4 \times 10^4$. The same qualitative behavior was obtained when ten random points within the chaotic regions were used as initial conditions to calculate particle trajectories. On the contrary, projections of particle trajectories at $Ra = 8.5 \times 10^4$ present different behavior depending on the initial condition. Figures 9(b-d) show the three qualitatively different behavior that were observed for particle trajectories initiated at points with coordinates $(0.15, -0.25, -0.5+0.05k),\ k = 1, \cdots, 19$. In particular, figure 9(b) shows that the projection of the particle trajectory is mostly confined within the region delimited by the boundary and several critical points. The trajectory shown in figure 9(c) tends to fill almost all the region $x+y \leq 0$ whereas that shown in figure 9(d) fills only two regions; the region shown in figure 9(b) and the symmetric region obtained by reflection with respect the diagonal $x-y=0$. Furthermore, the projection onto $z=0$ of the nine trajectories initiated at $(x,y,z) = (0.15, -0.25, -0.5+0.1k),\ k = 1, \cdots, 9$ are shown in figure 10(a). This figure reveals a higher density of points within the region filled by the streamline in figure 9(b). This higher density indicates that most of the streamlines tend to remain within this region most of the time. Figure 10(b) shows that an equivalent behavior is obtained when the initial points are chosen within the central triangular region delimited by the boundary and several critical points. It can be checked that some initial points give rise to orbit in tori, as it can be inferred from the projections. All particle trajectories shown in figures 9 and 10 were obtained by integrating an initial condition until time reached 10^3. Figures 9(b) and 10 suggest that surfaces of locally minimal geometric flux (see [18]) might exist. The existence of these surfaces would bound the rate of transport and consequently would explain the decrease of the maximal Lyapunov exponent observed in figure 6. The existence of surfaces with locally minimal flux and the role of critical points in their formation is beyond the scope of the current study and will be the subject of future research.

3.2. *Critical points*

The knowledge of the location and stability character of critical points of the flow is crucial to understand the 3D topology of flow patterns ([18], [19]). Table 2 shows the variation in the number of identified critical points, including critical points at the walls and edges of the cube, along the B_2 solution branch. Critical points are classified according to their stability character. Because of the volume preserving condition, only four types of non-degenerate critical points are possible; stable focus with a 1D unstable manifold (SF), unstable focus with a 2D unstable manifold (UF), saddle with a 2D unstable manifold and a 1D stable manifold (2S), and saddle with a 1D stable manifold and a 2D stable manifold (1S). Note that the Poincaré–Hopf index theorem is fulfilled in all cases listed in table 2 thus suggesting that no obvious critical point has been missed out.

As proposed by MacKay [18], sketches, known as flow skeletons, that show the critical points and some particle trajectories, can be very useful to understand the 3D spatial configuration and the mixing properties of the flow. Flow skeletons are presented in figures 11 and 12. Critical points and limiting streamlines on both the horizontal bottom wall, $z = -0.5$ and the lateral wall $x = -0.5$ are shown in figure 11. Critical points plotted in figure 11 are labeled according to their type. In addition, arrows indicating the stable and unstable direction of saddle points are included. Note that limiting streamlines on the rest of walls can be obtained from those presented in figure 11 by using the symmetry properties of the B_2 solution. Figure 12 shows the identified critical points and several particle trajectories on the symmetry invariant plane Π defined by $x + y = 0$. The evolution of the spatial configuration of the B_2 solution from a diagonal roll at $Ra = 10^4$ to a double–toroid at $Ra = 8.5 \times 10^4$, shown in figure 3 (a,b), is also evident in figures 11 and 12. Since this evolution can be associated to bifurcations of critical points, the current section is mainly devoted to the analysis of such bifurcations. It is worth to note that relevant bifurcations occur mostly in the symmetry invariant plane.

The more relevant bifurcations experimented by critical points inside the cavity are shown in figure 13, where the location and character of critical points are presented. In this figure critical points are labeled with a number in order to facilitate the identification of bifurcations. Those values of Ra where some changes in the number or stability character of critical points have been first detected along the continuation path are shown in figure 13. All the bifurcations of critical points identified inside the cavity are listed in table 3.

Secondary vortical structures that develop near two opposite edges shown in figure 3(a) are related to the unstable focus labeled 3 in figure 13(a). Tables 2 and 3 show that both the unstable focus 3 and the saddle with two unstable directions (2S) shown in figure 11(a) vanish at $Ra \in \left[2.7 \times 10^4, 2.8 \times 10^4\right]$. Table 2 also shows that the stable focus shown in figure 11(b) at $Ra = 10^4$ becomes a saddle with two stable directions at the bifurcation occurring at $Ra \in \left[4 \times 10^4, 4.1 \times 10^4\right]$. The next relevant bifurcation takes place at $Ra \in \left[5.7 \times 10^4, 5.8 \times 10^4\right]$. Within this interval the stable foci labeled 4 in figure 13 become unstable and as a consequence four stable foci, labeled 5 in figure 13, develop. Note that these four stable foci are not in the symmetry plane Π. The existence of the four stable foci 5 is related to the appearance of the spherical–like regions of regular motion observed in figure 7(c). Figure 12(c) shows that the central elliptic recirculation around the critical point 1 is rather elongated in the diagonal direction and consequently the recirculation motions around the critical points 4 become more important. The bifurcation that occurs at $Ra \in \left[5.9 \times 10^4, 6 \times 10^4\right]$ is the first of a series of three bifurcations that lead the B_2 solution to adopt the double toroidal spatial configuration shown in figure 3(b). Tables 2 and 3 and figures 12(d) and 13(d) show that the unstable focus 1 bifurcates to a saddle with two stable directions at $Ra \in \left[5.9 \times 10^4, 6 \times 10^4\right]$. In addition, two saddles with one stable direction, which are labeled 6 in figure 13, originate at this bifurcation point. As it was pointed out above, this bifurcation might be related to the substantial variation of the characteristics of the periodic orbit shown in figure 5. Figures 12(e) and 13(e) show that the points with label 6, which were saddles initially, become unstable foci at $Ra \in \left[6 \times 10^4, 6.1 \times 10^4\right]$. Furthermore, table 2 shows that the critical point $2S$ in figure 11(d) bifurcates to a stable focus within the same interval. Finally, the unstable foci 6 become stable and as a consequence four unstable foci, labeled 7 in figure 13, emerge at $Ra \in \left[6.2 \times 10^4, 6.3 \times 10^4\right]$. Tables 2 and 3 show that several bifurcations occur along the bifurcation branch between $Ra = 6.3 \times 10^4$ in the upper branch (i.e., before the first turning point) and $Ra = 5.2 \times 10^4$ in the lower branch, before the second turning point. However, after these bifurcations, the number and type of critical points shown in figure 13(f) at $Ra = 6.3 \times 10^4$ are recovered at $Ra = 5.2 \times 10^4$ and remain unchanged for values of Ra up to 8.5×10^4, as shown in figures 12(g) and 13(g) and tables 2 and 3.

4. Conclusions and outlook

Methods of Dynamical Systems have been used to study the rich dynamics of particle trajectories in a Rayleigh-Bénard problem. A fairly complete description of the dynamics for a large domain of Ra has been obtained by using different numerical tools. Poincaré maps on different Poincaré sections have been used to clarify the global structure of the flows studied. The dynamics are characterized by regions with regular motion, where nested tori and periodic orbits develop, surrounded by regions of chaotic motion. The size and shape of regular regions have been numerically estimated. The size of chaotic region tends to increase rapidly as Ra is increased. As a consequence, the percentage of region where chaotic motion occurs is above 95% even at moderate Rayleigh numbers ($8 \times 10^4 < Ra < 1.5 \times 10^5$). The chaotic nature of the flows has been quantified by the maximal Lyapunov exponent and the metric entropy. A singular point analysis, both in the interior and on the boundary of the domain, has been performed. Bifurcations of singular points have also been determined as a function of Ra. It was found that important changes on the topology and on the chaotic level of the flows were related to bifurcations of singular points. The main conclusion is that this methodology seems suitable to analyze similar problems.

The final goal of the current research is the design of flow configurations where mixing is greatly enhanced in the absence of mechanical devices. The dynamical systems tools used in the present study provide a detailed knowledge of the properties of the flow that can be used to select the parameter ranges where chaotic advection dominates.

Future work shall be addressed to study the relative position of the most relevant invariant manifolds of the fixed points and hyperbolic periodic orbits, to clarify the irregularities in the behavior of the maximal Lyapunov exponent. An extension to non-stationary flows (e.g. appearing at the Hopf points in figure 2) is also foreseen.

Acknowledgments

The authors D. P., J. H. and F. G. are grateful for the financial support received from DGIC project FIS2005-07194 and from the CIRIT "Programa de Grups de Recerca Consolidats de la Generalitat de Catalunya", project 2005SGR-00735. F. G. acknowledges the support received from the *Distinció a la Recerca de la Generalitat de Catalunya*. C. S. has been supported by grants MTM2006-05849/Consolider (Spain) and CIRIT 2005SGR-1028 (Catalonia). The computing facilities provided by the Departments of the authors have been largely used.

References

[1] G. O. Fountain, D. V. Khakhar, I. Mezic, J. M. Ottino, Chaotic mixing in a bounded three–dimensional flow, J. Fluid Mech. 417 (2000) 265–301.
[2] H. Aref, Stirring by chaotic advection, J. Fluid Mech. 143 (1984) 1–21.
[3] H. Aref, The development of chaotic advection, Phys. Fluids 14 (2002) 1315–1325.
[4] P. Ashwin, G. P. King, A study of particle paths in non–axisymmetric Taylor–Couette flows, J. Fluid Mech. 338 (1997) 341–362.
[5] R. Bachelard, T. Benzekri, C. Chandre, X. Leoncini, M. Vittot, Targeted mixing in an array of alternating vortices, Physical Review E 76 (2007) 046217.
[6] J. H. E. Cartwright, M. Feingold, O. Piro, An introduction to chaotic advection, in: H. Chaté, E. Villermaux, J. M. Chomez (Eds.), Chaos and Turbulence, Kluwer, 1999, pp. 307–342.
[7] L. Cortelezzi, A. Adrover, M. Giona, Feasibility, efficiency and transportability of short-horizon optimal mixing protocols, J. Fluid Mech. 597 (2008) 199–231.
[8] T. C. Lackey, Numerical investigation of chaotic advection in three–dimensional experimentally realizable rotating flows, Ph.D. thesis, Georgia Institute of Technology, Georgia. USA (2004).
[9] I. Mezic, F. Sotiropoulos, Ergodic theory and experimental visualization of invariant sets, Phys. Fluids 14 (2002) 2235–2243.
[10] J. M. Ottino, Mixing, chaotic advection and turbulence, Annu. Rev. Fluid Mech. 22 (1990) 207–253.
[11] F. Sotiropoulos, Y. Ventikos, T. C. Lackey, Chaotic advection in three-dimensional stationary vortex-breakdown bubbles: Sil'nikov's chaos and the devil's staircase, J. Fluid Mech. 444 (2001) 257–297.
[12] D. Puigjaner, J. Herrero, C. Simó, F. Giralt, Bifurcation analysis of steady Rayleigh–Bénard convection in a cubical cavity with conducting sidewalls, J. Fluid Mech. 598 (2008) 393–427.
[13] D. Puigjaner, J. Herrero, F. Giralt, C. Simó, Bifurcation analysis of multiple steady flow patterns for Rayleigh–Bénard convection in a cubical cavity at $pr = 130$, Physical Review E 73 (2006) 046304.
[14] D. Puigjaner, J. Herrero, F. Giralt, C. Simó, Stability analysis of the flow in a cubical cavity heated from below, Phys. Fluids 16 (2004) 3639–3655.
[15] V. I. Arnold, A. Avez, Problèmes ergodiques de la mécanique classique, Gauthier-Villars, Paris, 1967.
[16] J. Jeong, F. Hussain, On the identification of a vortex, J. Fluid Mech. 285 (1995) 69–94.
[17] C. Simó, A. Vieiro, Some relevant aspects of area preserving maps and the planar conservative Hénon map, work in progress.
[18] R. S. MacKay, Transport in 3d volume–preserving flows, J. Nonlinear Sci. 4 (1994) 329–354.
[19] A. E. Perry, M. S. Chong, A description of eddying motions and flow patterns using critical–points concepts, Annu. Rev. Fluid Mech. 19 (1987) 125–155.

Solution	Generators of the symmetry group	Range of stability
B_2	S_{d_-}, $-I$	$67\,730 - 85\,694$
B_{25}	$-I$	$85\,694 - 87\,598$
B_{251}	S_y, $-I$	$61\,160 - 65\,297$ $87\,598 -$

Table 1
Symmetry properties and ranges of stability of the studied solutions. S_y, S_{d_-} refer to reflections about the planes $y = 0$ and $x + y = 0$, respectively. The symmetry with respect to the origin is denoted as $-I$.

		Interior				**Walls**			**Edges**	
K	$10^{-3}Ra$	SF (2)	UF (-2)	2S (2)	1S (-2)	SF (1)	2S (1)	1S (-1)	2S (1)	1S (-1)
0	10	2	3	2	0	4	2	6	0	2
1	11	2	3	0	0	4	2	2	2	4
2	28	2	1	0	0	4	0	2	0	4
3	41	2	1	0	0	0	4	2	0	4
4	58	4	3	0	0	0	4	2	0	4
5	60	4	2	1	2	0	4	2	0	4
6	61	4	4	1	0	4	0	2	0	4
7	63	6	6	1	0	4	0	2	0	4
8	65	6	6	1	0	4	2	4	0	4
9	68.58	6	6	2	1	4	2	4	0	4
10	68.71	6	6	2	1	4	6	8	0	4
11	68	6	6	1	0	8	2	8	0	4
12	58	6	6	1	0	8	0	6	0	4
13	57	6	6	1	0	4	4	6	0	4
14	52	6	6	1	0	4	0	2	0	4

Table 2
Number of critical points, classified according to their location (in the interior of the cube, at the walls or edges) and their type, i.e., stable focus (SF), unstable focus (UF), saddle with two stable directions (2S) and saddle with one stable direction (1S). The respective contributions to the sum of Poincaré indexes is given in parenthesis. The table lists the Rayleigh numbers that follow each bifurcation detected along the continuation path. The initial case with Ra $= 10^4$ is also included in the table.

Label	K_s	K_e	Type	(x_s, y_s, z_s)	(x_e, y_e, z_e)
1	0	5	UF	(0,0,0)	(0,0,0)
	5	9	2S		
	9	11	1S		
	11	-	2S		
2	0	0	2S	(0.488,-0.488,0.230)	(0.488,-0.488,0.230)
3	0	2	UF	(-0.443,0.443,-0.418)	(-0.499,0.499,-0.499)
4	0	4	SF	(0.368,-0.368,-0.289)	(0.278,-0.278,-0.263)
	4	-	UF	(0.273,-0.273,-0.260)	(0.196,-0.196,-0.178)
5	4	-	SF	(0.204,-0.331,-0.264)	(-0.065,-0.420,-0.280)
6	5	5	1S	(0.040,-0.040,0.051)	(0.040,-0.040,0.051)
	6	7	UF	(0.121,-0.121,0.162)	(0.131,-0.131,0.183)
	7	-	SF	(0.135,-0.135,0.194)	(0.299,-0.299,0.275)
7	7	-	UF	(0.082,-0.172,0.187)	(0.235,0.079,0.196)
8	9	11	2S	(0.026,0.026,0)	(0.027,0.027,0)

Table 3
Characteristics of the interior critical points. The first column lists the labels associated to each critical point. The second and third columns respectively show the case (in relation with the row indexes of table 1) where the point is first observed and the case where it is not detected anymore. The fourth column shows the type of fixed point according to its stability properties, i.e., stable focus (SF), unstable focus (UF), saddle with two stable directions (2S) and saddle with one stable direction (1S). Note that a given fixed point may vary its stability properties one or more times along the continuation path. The fifth column shows the coordinates of the location where the fixed point is first detected and the last column shows the location where the fixed point was last observed.

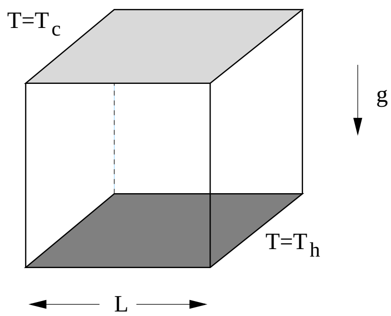

Fig. 1. A sketch of the cubical cavity.

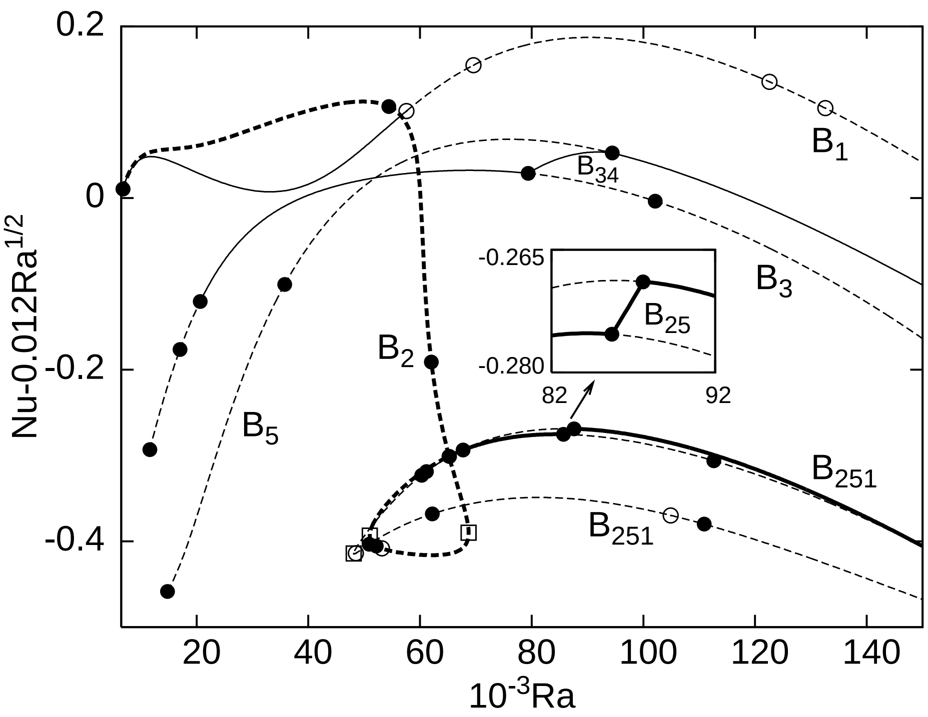

Fig. 2. Bifurcation diagram of seven steady solutions, B_1, B_2, B_3, B_5, B_{25}, B_{34} and B_{251} at $Pr = 130$. Stable and unstable flow patterns are respectively depicted with solid and dashed lines. Steady bifurcations, Hopf bifurcations and turning points are represented by filled circles, hollow circles and hollow squares, respectively. An additional magnification of the smaller domain of existence for the B_{25} solution is also included. The solutions that are object of the current study are highlighted with thick lines.

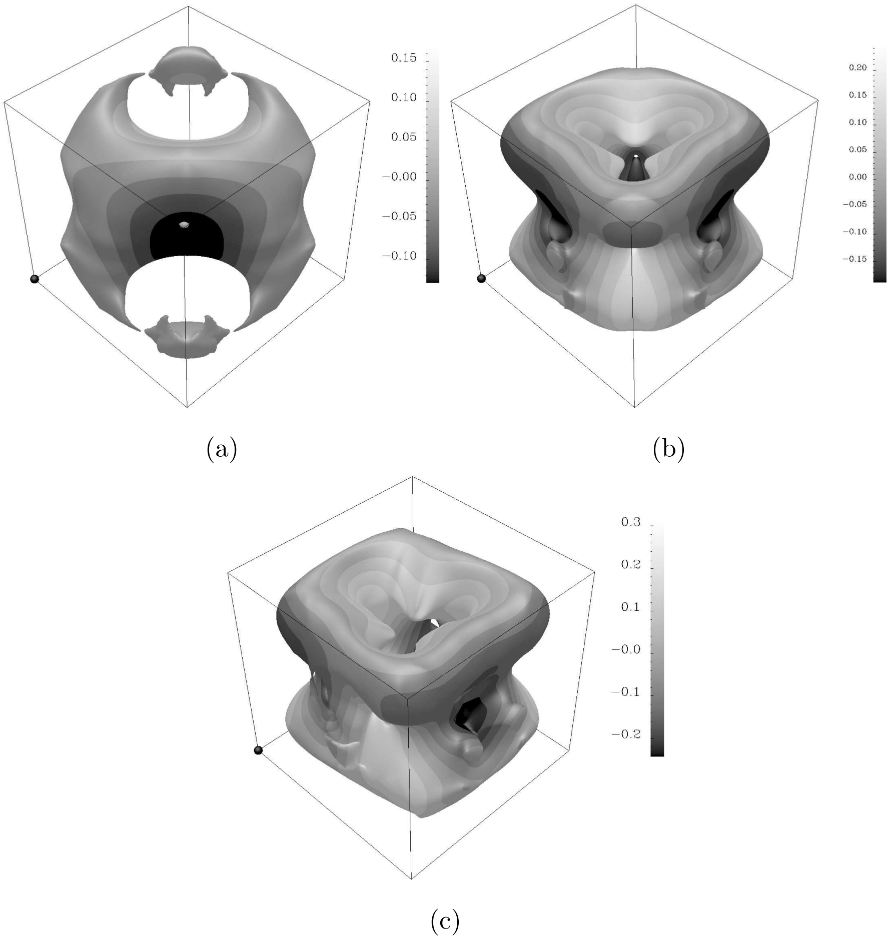

Fig. 3. Surface of the second largest eigenvalue (Λ_2) of the tensor $S^2 + \Omega^2$, formed from the symmetric (S) and antisymmetric (Ω) parts of the velocity gradient tensor for (a) the unstable B_2 flow pattern at $Ra = 10^4$, (b) the stable B_2 flow pattern at $Ra = 85\,000$ and (c) the stable flow pattern B_{251} at $Ra = 10^5$. The grey levels are scaled with the value of the vertical velocity component and the filled circles denote the vertex with coordinates $(-0.5, -0.5, -0.5)$ while the coordinates of the lower frontal vertex are $(0.5, -0.5, -0.5)$.

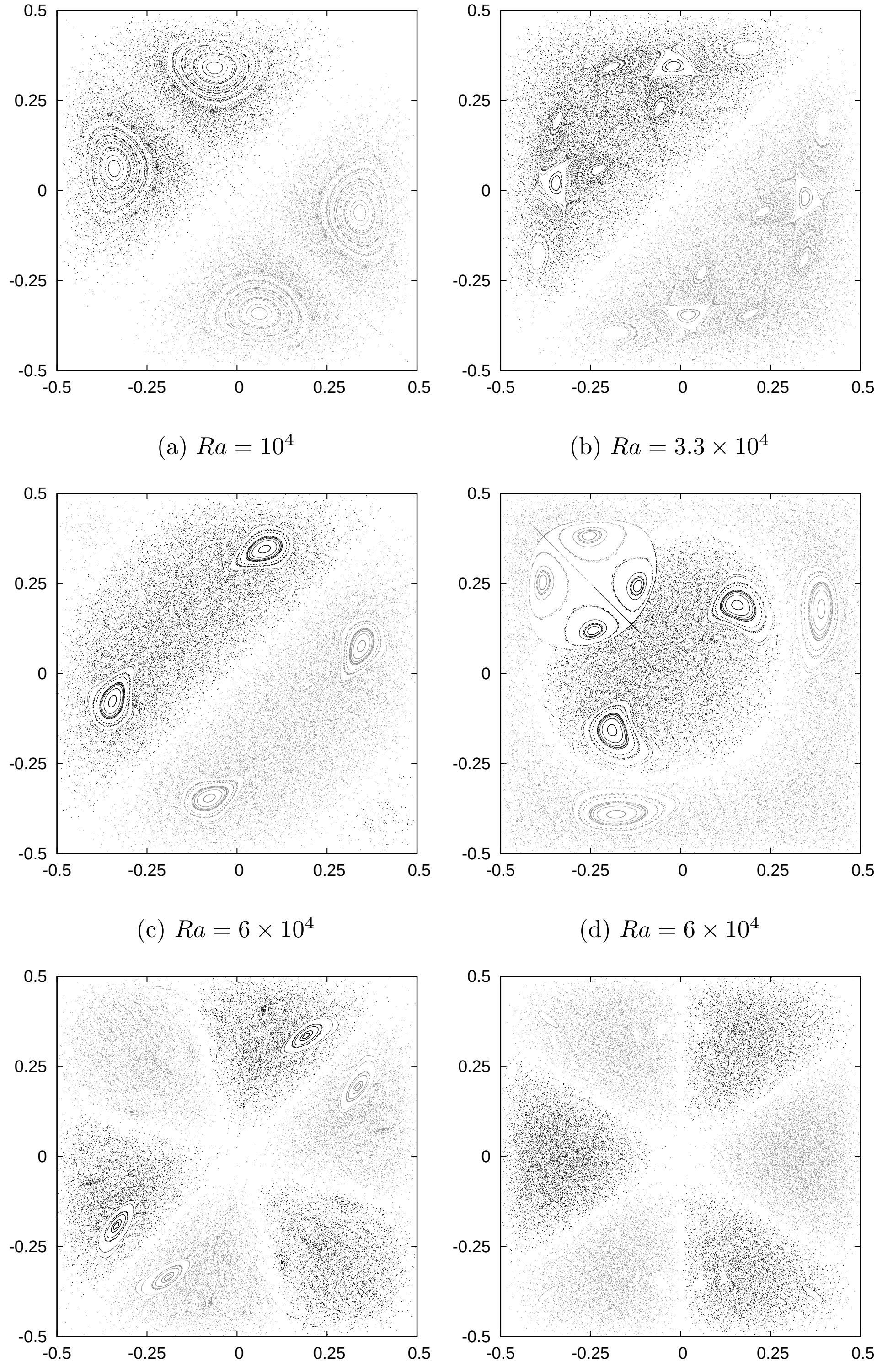

(a) $Ra = 10^4$ (b) $Ra = 3.3 \times 10^4$

(c) $Ra = 6 \times 10^4$ (d) $Ra = 6 \times 10^4$

(e) $Ra = 8.5 \times 10^4$ (f) $Ra = 10^5$

Fig. 4. (a-e) Poincaré maps for the B_2 solution at different Rayleigh numbers. (f) Poincaré maps for the B_{251} solution at $Ra = 10^5$. The horizontal midplane $z = 0$ is used as Poincaré section in all the plots except in plot (d) where the Poincaré map at the plane $z = 0.4$ is represented. Black and grey points represent intersections of trajectories with positive and negative vertical velocity component, respectively.

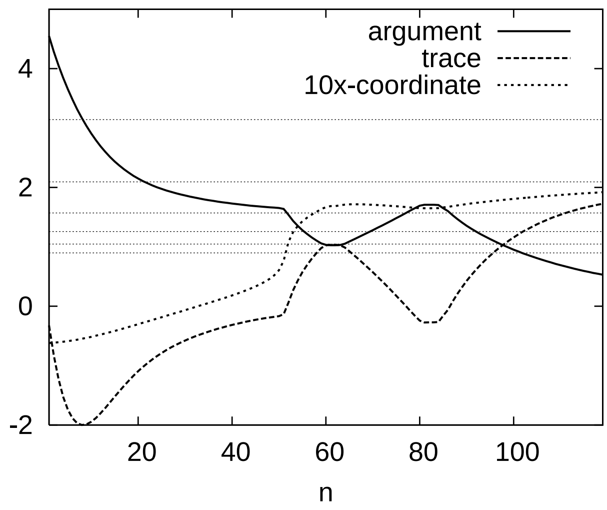

Fig. 5. Variation of the x coordinate of the main elliptic fixed point of the Poincaré map at $z = 0$ for the B_2 solution along the continuation branch. The variation of the trace of the differential of the Poincaré map and of the argument of the complex conjugate eigenvalues associated to the elliptic point are also plotted. Since the continuation branch has two turning points the number of studied solution n has been used as abscissa instead of Ra. The x coordinate is multiplied by ten in the figure to fit the vertical coordinate range of the other two plotted curves. Since islands of period k originate or end whenever the argument curve intersects the $y = 2\pi/k$ line, the horizontal lines $y = 2\pi/k$, $k = 2, \ldots, 7$, are included in the plot.

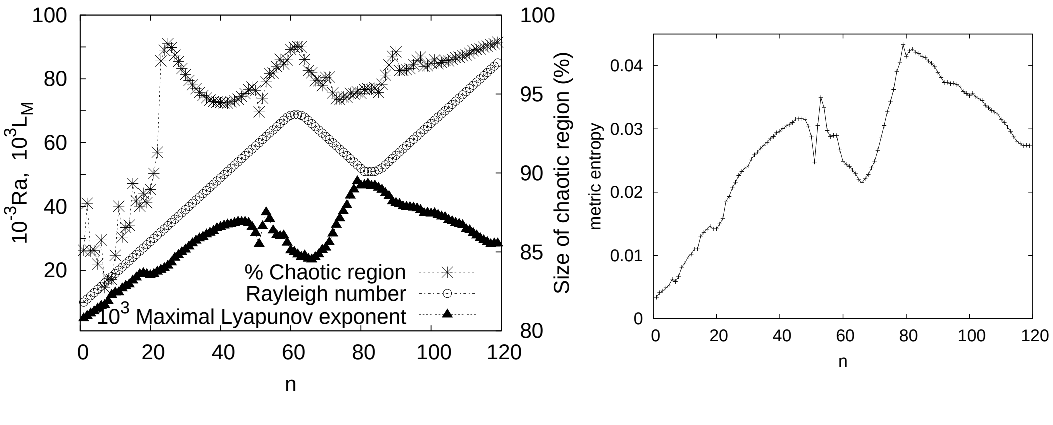

(a)

(b)

Fig. 6. (a) Variation of the maximal Lyapunov exponent and of the percentage of chaotic region $100V_c$ for the B_2 flow pattern. Since the B_2 solution branch presents two turning points, the number of studied solution, n, has been used as ordinate instead of the Rayleigh number. A curve relating n with the corresponding Ra value has also been included in the figure. The y-axis of the curve that shows the variation of the percentage of chaotic region has to be read on the right side of the plot. (b) Metric entropy $h_m = L_M \times V_c$ as a function of the index n.

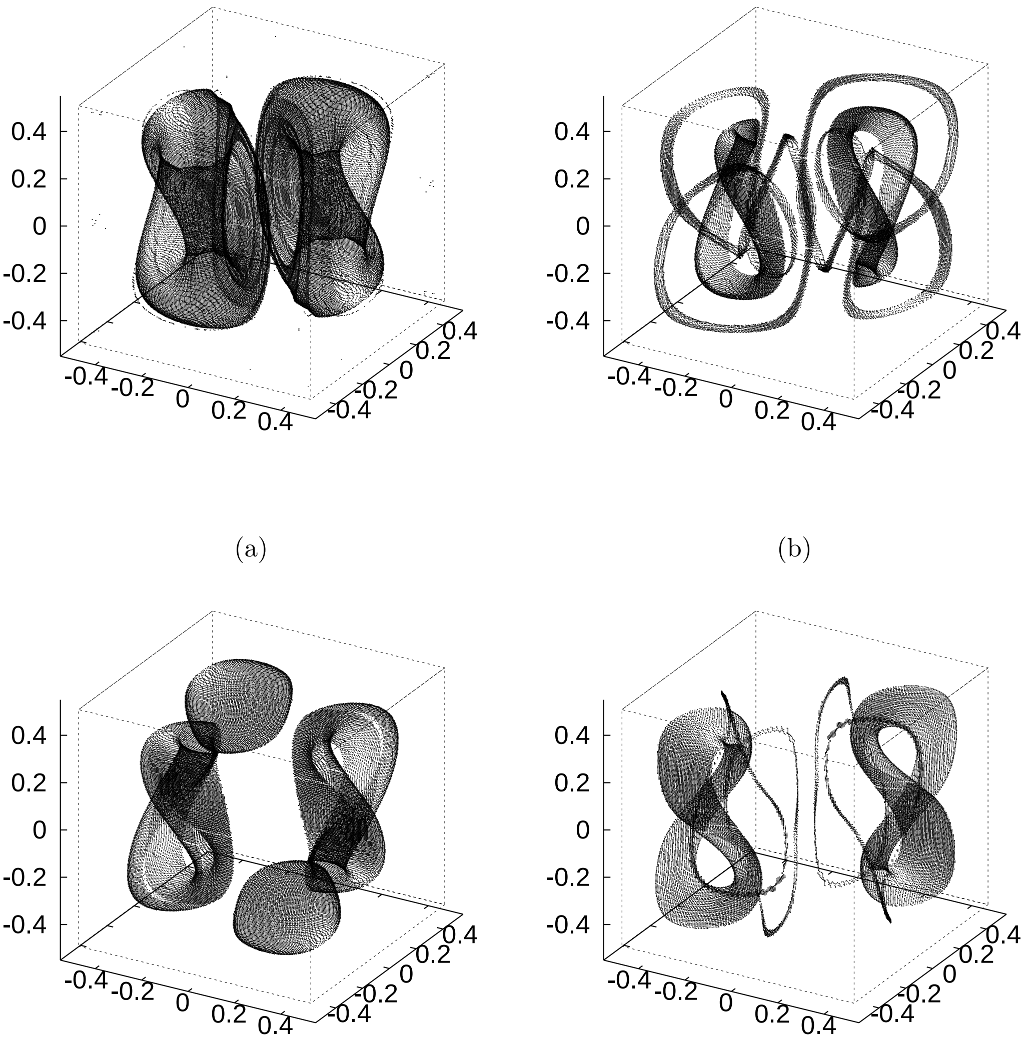

(a) (b)

(c) (d)

Fig. 7. Regions with regular motion for the B_2 branch of solutions at (a) $Ra = 10^4$, (b) $Ra = 3.4 \times 10^4$, (c) $Ra = 6 \times 10^4$, and (d) $Ra = 8.5 \times 10^4$. Only points at the boundaries of the domains confined by invariant tori are displayed at the resolution of the pixels.

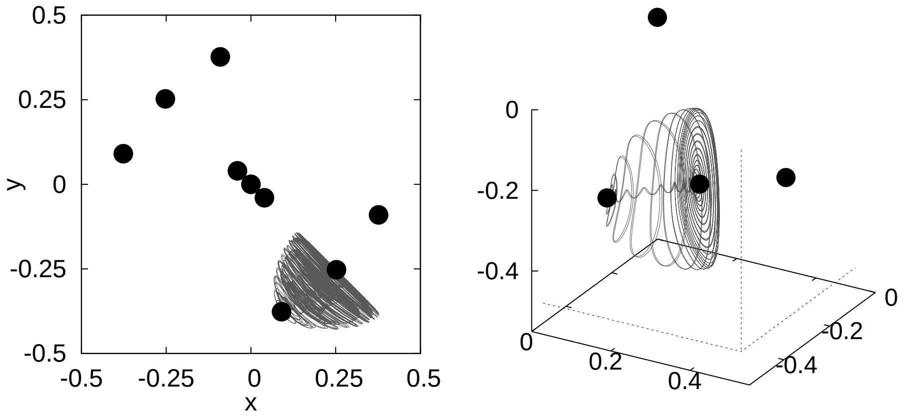

(a) (b)

Fig. 8. Particle trajectories for the B_2 solution at $Ra = 6 \times 10^4$ and initial conditions within one regular spherical–like region shown in figure 7(c). (a) Projection onto the plane $z = 0$ of three particle trajectories. (b) 3D view of one particle trajectory. Critical points are represented with filled circles.

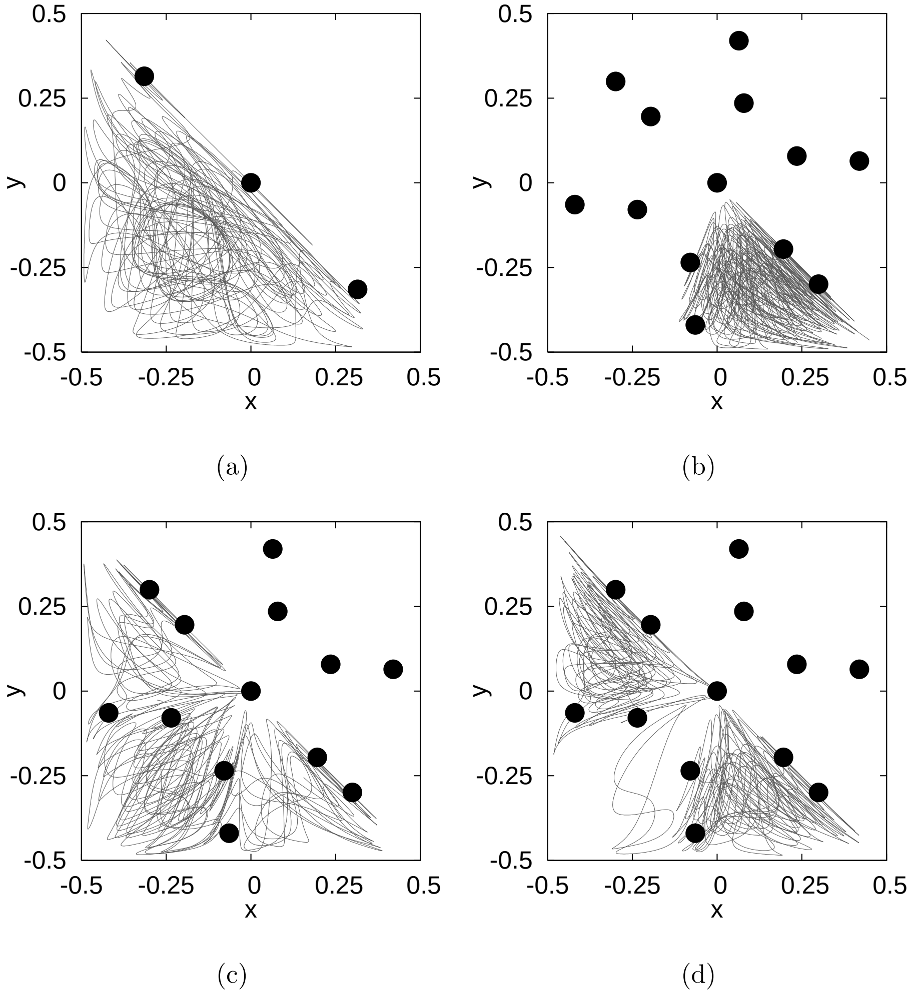

Fig. 9. Projection onto the midplane $z = 0$ of one particle trajectory of the B_2 solution and of all identified critical points inside the cavity at (a) $Ra = 4 \times 10^4$, (b-d) $Ra = 8.5 \times 10^4$.

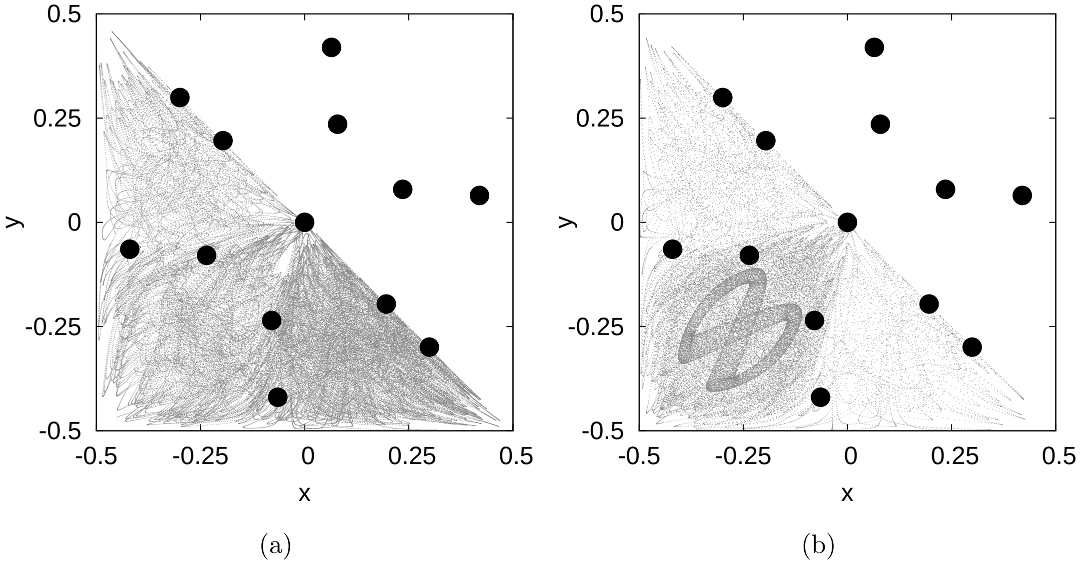

Fig. 10. Projection onto the midplane $z = 0$ of nine particle trajectories for the B_2 solution at $Ra = 8.5 \times 10^4$. Initial conditions were of the form (a) $(0.15, -0.25, -0.5 + 0.1k),\ k = 1, \cdots, 9$; (b) $(-0.25, -0.25, -0.5 + 0.1k),\ k = 1, \cdots, 9$.

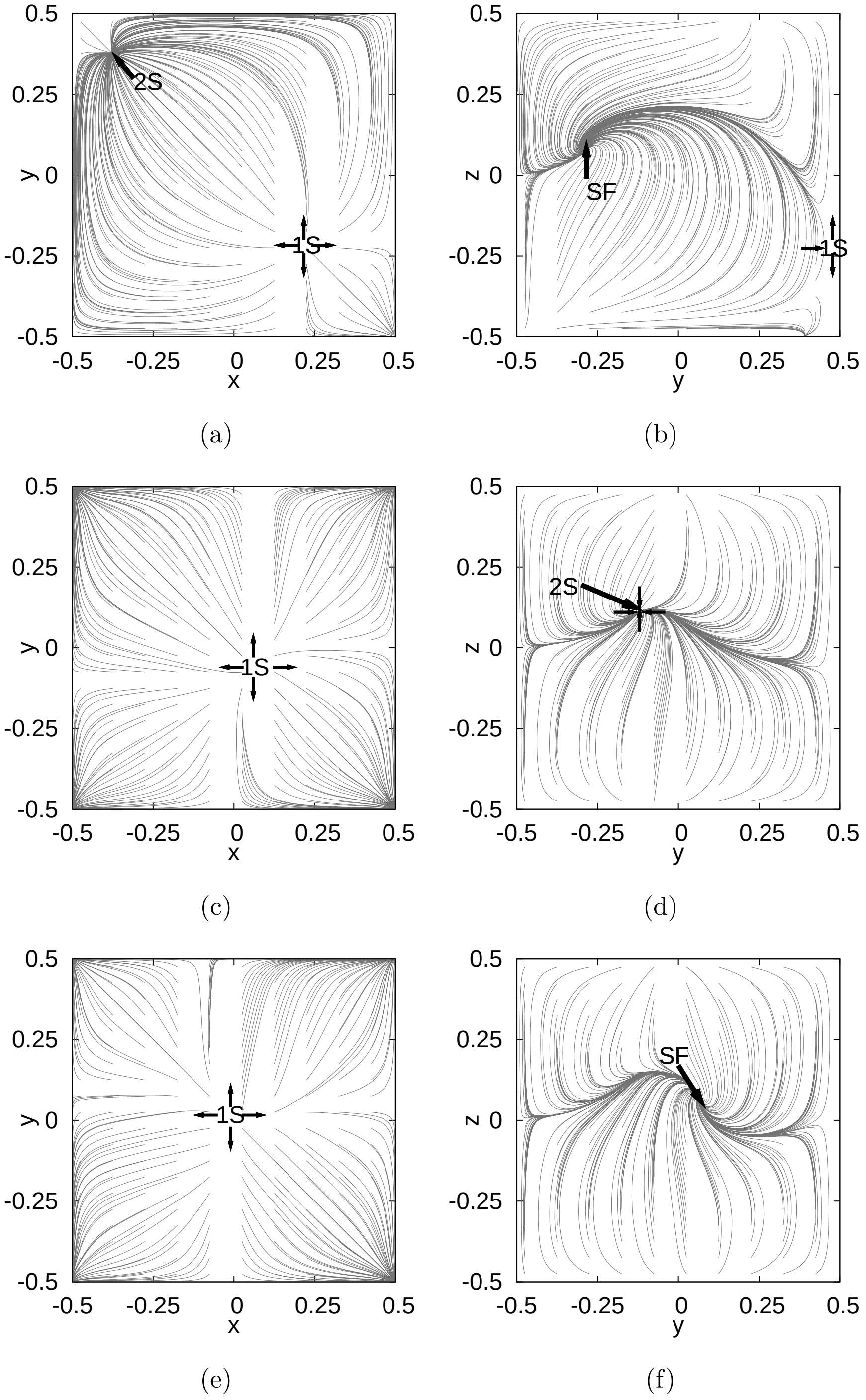

Fig. 11. Limiting streamlines for the B_2 solution at the bottom wall $z = -0.5$ (a,c,e) and at the lateral wall $x = -0.5$ (b,d,f). The Rayleigh number is 10^4 in plots (a) and (b), 6×10^4 in plots (c) and (d) and 8.5×10^4 in plots (e) and (f).

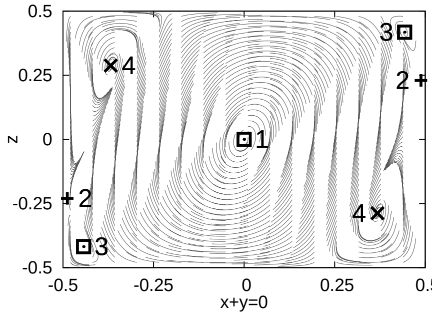

(a) $Ra = 10^4$

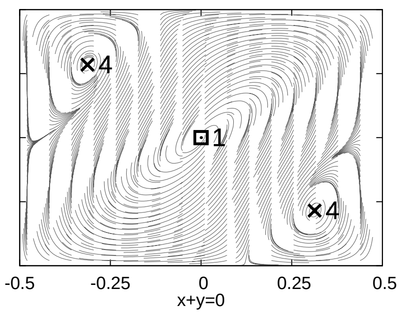

(b) $Ra = 4.1 \times 10^4$

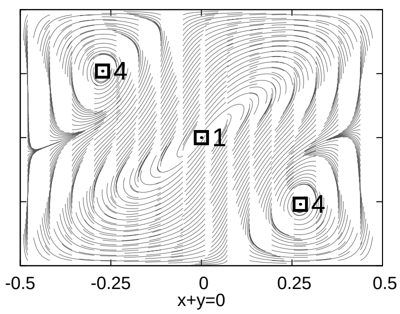

(c) $Ra = 5.8 \times 10^4$

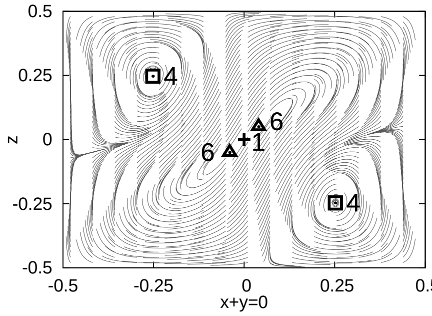

(d) $Ra = 6 \times 10^4$

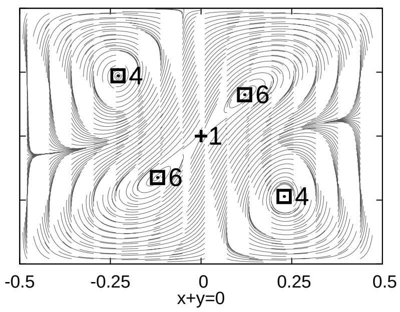

(e) $Ra = 6.1 \times 10^4$

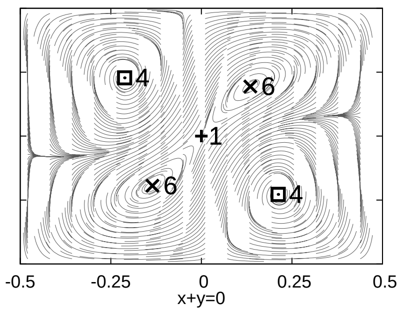

(f) $Ra = 6.3 \times 10^4$

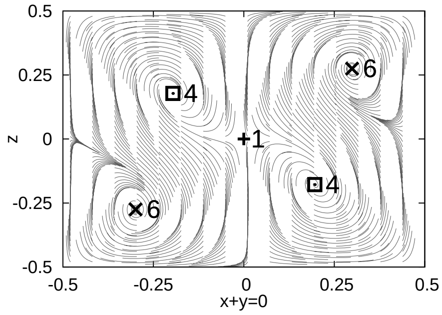

(g) $Ra = 8.5 \times 10^4$

Fig. 12. Particle trajectories and critical points on the invariant symmetry plane Π , defined by $x+y=0$, for the B_2 solution. Stable focus (SF), unstable focus (UF), saddles with two stable directions (2S) and saddles with one stable direction (1S) are plotted with crosses, squares, plus signs and triangles, respectively.

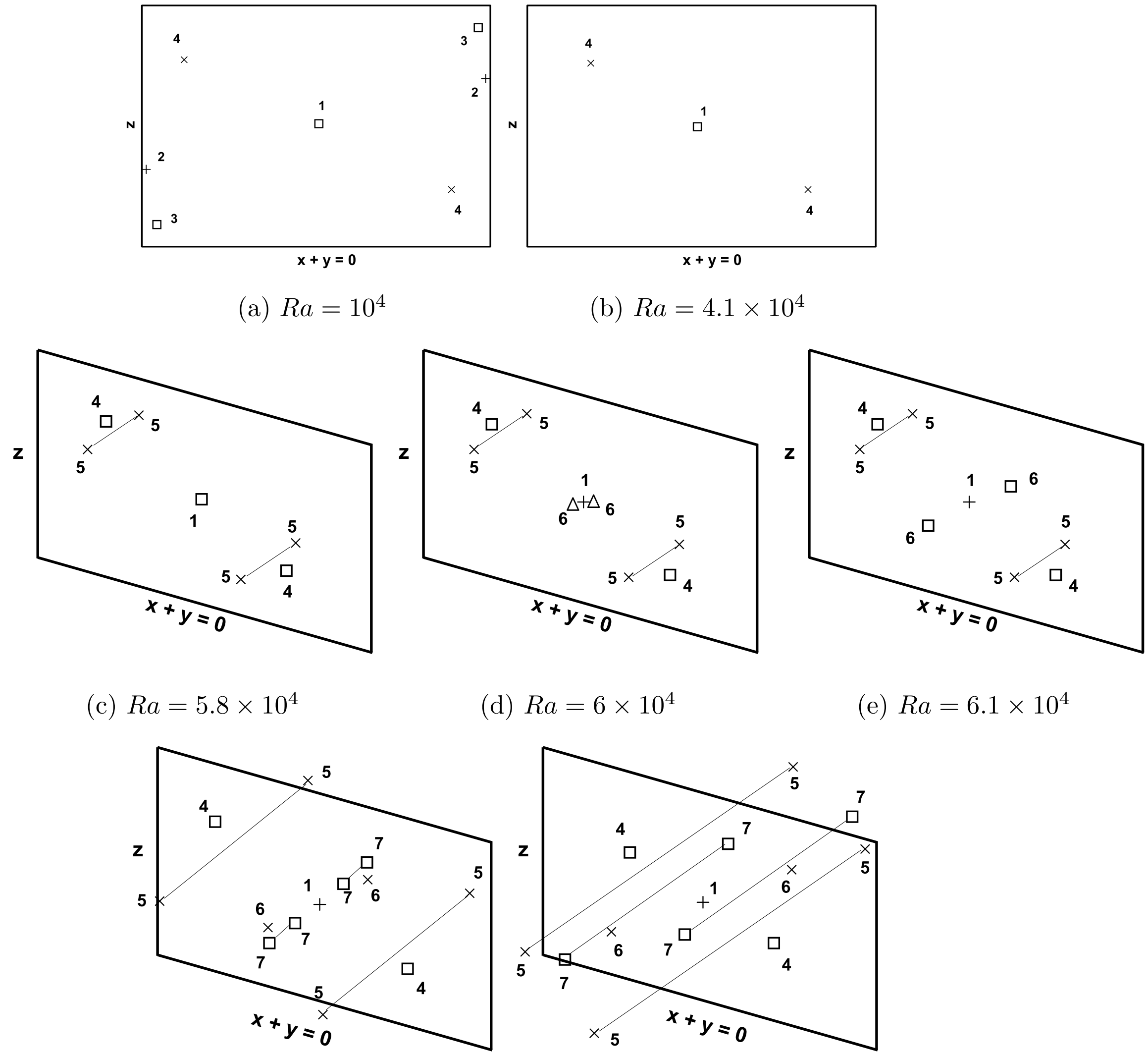

(a) $Ra = 10^4$ (b) $Ra = 4.1 \times 10^4$

(c) $Ra = 5.8 \times 10^4$ (d) $Ra = 6 \times 10^4$ (e) $Ra = 6.1 \times 10^4$

(f) $Ra = 6.3 \times 10^4$ (g)$Ra = 8.5 \times 10^4$

Fig. 13. Location and character of the identified critical points inside the cube for the B_2 solution. Critical points that are not in the invariant symmetry plane $x + y = 0$ and that are symmetric w.r.t. this plane are joined with thin lines.